Nucleic Acids Research, 2025, **53**, gkaf443
https://doi.org/10.1093/nar/gkaf443
Nucleic Acid Enzymes

A conserved nuclease facilitates environmental DNA uptake

Juri Hanßmann[1,2,†], Jan Pané-Farré[3,5,†], Milena Meiser[3], Mathias Girbig[2], Lifei Fu[4], M. Gregor Madej[4], Franziska L. Sendker[2], Clemens Thölken[5], Marcus Lechner[5], Christine Ziegler[4], Georg K.A. Hochberg[1,2], Gert Bange[2,3,5], Martin Thanbichler[1,2,5], Rebecca Hinrichs[3,5,*,†]

[1]Department of Biology, University of Marburg, 35043 Marburg, Germany
[2]Max Planck Institute for Terrestrial Microbiology, 35043 Marburg, Germany
[3]Department of Chemistry, University of Marburg, 35043 Marburg, Germany
[4]Department of Biophysics II, University of Regensburg, 93053 Regensburg, Germany
[5]Center for Synthetic Microbiology (SYNMIKRO), University of Marburg, 35043 Marburg, Germany

[*]To whom correspondence should be addressed. Email: rebecca.hinrichs@synmikro.uni-marburg.de
[†]These authors should be regarded as Joint Authors.

Abstract

Bacteria acquire new traits through the uptake of genetic material from the environment, a process requiring DNA processing. However, the molecular inventory mediating this process is far from being completely understood. Here, we identify YhaM in *Bacillus subtilis* as a conserved 3′-deoxyribonuclease essential for the uptake and processing of genetic information in the form of single-stranded DNA. Our results show that YhaM assembles into hexamers in the presence of divalent cations, enhancing substrate binding, which is achieved through its conserved oligonucleotide-binding domain. Cells lacking YhaM show a severe defect in the uptake of plasmids and genomic DNA, but the transduction of double-stranded DNA by the phage SPP1 remains unaffected. These findings highlight a critical role of YhaM in single-stranded DNA maturation during natural transformation. Importantly, this function is conserved in various Gram-positive human pathogens such as *Staphylococcus aureus*, suggesting that it could contribute to the spread of antibiotic resistance.

Graphical abstract

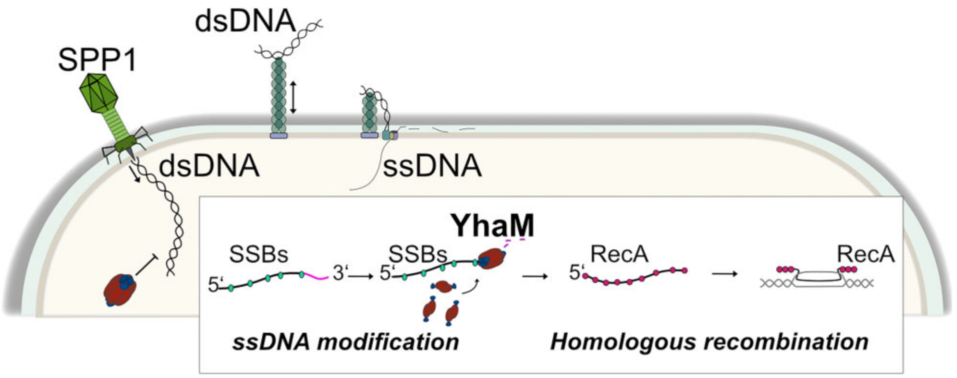

Introduction

The ability of naturally competent bacteria to take up environmental DNA (transformation) poses a significant public health risk. In pathogenic species, this process promotes the acquisition of genetic elements encoding antibiotic resistance and virulence factors and facilitates metabolic adaptations, thereby contributing to the emergence and persistence of multidrug-resistant organisms [1, 2]. Despite extensive research on bacterial transformation, the molecular mechanisms underlying DNA processing during uptake remain poorly understood. Of particular interest is the unclear function of nucleases in dealing with single-stranded DNA (ssDNA) intermediates [3].

In naturally competent bacteria, DNA uptake occurs via type IV-like pili that capture and transport double-stranded DNA (dsDNA) into the periplasm [3–5]. After uptake, dsDNA is divided into two single strands: one strand is degraded,

Received: March 13, 2025. **Revised:** April 14, 2025. **Editorial Decision:** April 16, 2025. **Accepted:** May 13, 2025

while the other is transported into the cytosol through a membrane channel protein, entering with its 3′ end first [3, 6]. In the cytoplasm, the imported ssDNA is immediately coated by SsbA and SsbB, which protect it from nucleases and temporarily inhibit RecA binding [7]. During chromosomal transformation, DprA and RecO interact with the ssDNA to facilitate RecA loading and enable homologous recombination with the chromosome [8, 9]. In contrast, the establishment of a self-replicating plasmid requires different pathways that are independent of RecA [10]. Beyond its role in recombination, RecA also links competence to the bacterial SOS response by promoting LexA repressor cleavage, thereby activating DNA repair pathways. In some species, such as *Streptococcus pneumoniae*, competence can even substitute for the SOS response by providing template DNA for recombinational repair, further highlighting the connection between horizontal gene transfer (HGT) and DNA repair [11–13]. Although the conjugation and recombination processes have been studied intensively, it remains unclear whether ssDNA needs to be processed by nucleases immediately after its uptake to prepare it for cellular use [3, 14].

Here, using the model organism *Bacillus subtilis*, we identify YhaM as a conserved 3′-deoxyribonuclease essential for efficient transformation and a new player in DNA uptake. YhaM has been described as LexA-regulated 3′-exoribonuclease that is highly conserved in Gram-positive bacteria [15] but also present in some Gram-negative bacteria and archaea [16]. Our structural and biochemical analyses reveal that YhaM forms a hexameric deoxyribonuclease ring composed of a trimer of dimers that assembles around ssDNA and dsDNA. The absence of YhaM leads to a substantial reduction in transformation efficiency, indicating a central role for this ssDNA-specific 3′-deoxyribonuclease in DNA uptake and processing. By investigating its functional role and molecular mechanism, we provide new insights into DNA processing during natural competence, with implications for HGT in Gram-positive pathogens such as *Staphylococcus aureus*.

Materials and methods

Growth conditions

The bacterial strains, plasmids, and oligonucleotides used in this study are listed in Supplementary Tables S3–S6. LB (lysogeny broth) medium or plates solidified with 1.5% Bacto agar at 37°C were used to cultivate *Escherichia coli* and *B. subtilis* strains. When appropriate, antibiotics were included at the following concentrations: ampicillin 100 μg/ml, chloramphenicol 5 μg/ml, spectinomycin 100 μg/ml, and kanamycin 30 μg/ml. Isopropyl-β-D-thiogalactopyranoside (IPTG, Sigma) was added to the medium at the indicated concentration when appropriate. The wild-type *B. subtilis* host was DK1042 (*comI*$^{\mathrm{Q12L}}$) [17], a genetically competent derivative of *B. subtilis* NCIB 3610.

Plasmids and strains

All constructs were initially introduced into the domesticated strain PY79 via natural competence and then transferred to the DK1042 background using SPP1-mediated generalized phage transduction [18]. The *yhaM::kan* insertion was generated using SPP1 phage lysate of donor strains obtained from the Bacillus Genetic Stock Center (BKK09930) (Columbus, OH, USA) [19]. To induce *yhaM*, the strains were transformed with pDR111 [20] derivatives. The plasmid contains an IPTG-dependent $P_{hyper\text{-}spank}$ promoter flanked by the upstream and downstream regions of *amyE* for homologous recombination. For the construction of pDR111, a polymerase chain reaction (PCR) product was obtained using genomic DNA (gDNA) of strain DK1042 as a template. It contains the open reading frame of *yhaM* (or mutant alleles thereof) and 25 bp overhangs. After SalI/SphI restriction of the plasmid, the PCR fragment was inserted by Gibson assembly [21]. The constructs were validated by DNA sequencing. To create mNeongreen and mScarlet-I fusion proteins in *B. subtilis*, we used the CRISPR–Cas9 system [22]. The production of full-length YhaM-mNG was verified using Western blot analysis (Supplementary Fig. S2). Plasmids encoding C-terminally His$_6$-tagged proteins were constructed by amplifying gene fragments encompassing the genes of interest by PCR, followed by their insertion into the pET24d vector (Novagen) via BsaI restriction sites. *E. coli* DH5α was used for cloning purposes.

Overproduction and affinity purification of YhaM

Escherichia coli strain BL21(DE3) (Novagen) transformed with plasmid pET24d was used for protein production. Initially, the cells were cultured in LB medium for 3 h at 37°C with shaking at 180 rpm. Gene expression was induced by adding 0.25 mM IPTG, followed by a 14-h incubation at 22°C with agitation at 180 rpm. Cells were harvested by centrifugation (4000 rpm/3500 × *g* for 20 min at 4°C). Subsequently, the cell pellets were resuspended in lysis buffer (25 mM HEPES, at pH 8, 200 mM NaCl, 20 mM $MgCl_2$, 10 mM KCl) at a ratio of 25 ml per gram of cells and then processed using an M1-10L Microfluidizer (Microfluidics). After cell lysis, cell debris was removed by high-speed centrifugation, and the proteins were purified by nickel-ion affinity chromatography (FF-HisTrap columns; GE Healthcare). This was followed by an incubation step with ethylenediaminetetraacetic acid (EDTA) (0.5 M, 1.5 h, 20°C) and a second purification step by size exclusion chromatography in SEC buffer (20 mM HEPES, at pH 8, 200 mM NaCl, 20 mM KCl, and 20 mM $MgCl_2$). Elution fractions containing protein were concentrated by ultrafiltration using Amicon Ultracel-10K cells (Millipore). Fractions were analyzed by sodium dodecyl sulfate–polyacrylamide gel electrophoresis (SDS–PAGE) (Supplementary Fig. S4). Protein-containing fractions were pooled and concentrated according to experimental requirements. Protein concentrations were determined by spectrophotometry (NanoDrop; Thermo Scientific).

Cryo-EM grid preparation

3.5 μl of a YhaM solution (∼12 μM) in a buffer containing 25 mM Tris (pH 8.0), 200 mM NaCl, and 20 mM $MgCl_2$ was applied to Quantifoil R1.2/1.3 carbon-coated copper grids (300 mesh) and blotted with filter paper for 5.5 s before being plunge-frozen in liquid ethane with an automated Vitrobot IV.

Cryo-EM data collection

Cryo-electron microscopy (cyro-EM) data for the YhaM protein were collected using a JEOL CRYO ARM 200 electron microscope operating with an accelerating voltage of 200 keV and equipped with an energy filter and slit width of 20 eV. A total of 4304 movies were collected. Micrographs were recorded using a K2 Summit direct electron detector operating in counting mode at a calibrated pixel size of 0.7891 Å and a nominal magnification of 60 000×. The total electron dose was 57.21 e^- per $Å^2$, distributed over 53 frames during a total exposure time of 6.36 s. The defocus range was varied from −0.7 to −1.4 µm in 0.1 µm increments. A 3 × 3 beam shift pattern was utilized, with one exposure per hole. Real-time preprocessing and quality monitoring were conducted using cryoSPARC Live to ensure optimal data collection and microscope performance.

Data processing

Initial micrograph assessment revealed densely packed and evenly distributed particles, with an average of ~600 particles per micrograph. Motion correction and dose weighting were performed using MotionCor2, and contrast transfer function (CTF) parameters were estimated using CTFFIND4. Subsequent particle picking, 2D and 3D classification, and 3D refinement were conducted using RELION 5.0 and CryoSPARC 4.6.

After 3D classification in RELION, the particle dataset of 2402876 particles was refined to 1201417 particles. The initial 3D refinement was conducted under C1 symmetry operators (C1) without applying corrections, with CTF refinement implemented to address beam tilt, trefoil aberrations, and variations in per-particle defocus. Bayesian polishing was used to improve particle trajectories and enhance the signal-to-noise ratio. The polished particles were re-extracted into a 320-pixel box.

The 1201417 polished particles were then refined using nonuniform refinement in CryoSPARC, using the updated CTF parameters. This procedure resulted in consensus maps at resolutions of 3.82 Å (C1 symmetry) and 3.73 Å (D3 symmetry). Although the local resolution in the visible density regions reached 3.0–3.1 Å, the global resolution was limited by blurring near the hexameric ring surface, likely due to structural flexibility. To address this issue, particle subtraction was applied, removing poorly resolved areas near the surface using a solvent mask. After signal subtraction, the final particle set of 1168864 particles was refined to 3.77 Å (C1 symmetry) and 3.47 Å (D3 symmetry), with local resolution analysis indicating visible density regions between 2.9 Å and 3.1 Å. Orientation diagnostics using cFAR (0.84) indicated minimal anisotropy. To further enhance map interpretability for model building and visualization, local filtering and DeepEMhancer were applied. Resolution estimates were based on the gold-standard Fourier shell correlation at the 0.143 criterion.

Model building

The initial model generated by AlphaFold3 [23] was fitted to the nonuniformly refined and sharpened maps using UCSF Chimera and manually corrected in Coot. Amino acid assignments were verified based on the unique density of bulky side chains. Iterative rounds of real-space refinement of the entire complex were performed in PHENIX v1.21-5207 [24], with validation using Phenix validation tools. The atomic model was also validated using MolProbity [25] to assess the geometry and overall quality of the model. The resulting YhaM model coordinate file and the cryo-EM density maps were deposited at rcsb.org with the following accession codes: PDB ID 9H3F and EMD-51819.

Nuclease assays

6-Carboxyfluorescein (6-FAM)-labeled DNA or RNA oligonucleotides (Merck, Darmstadt, Germany) were used to generate nucleic acid substrates. The sequences of the substrates are listed in Supplementary Table S6. Nuclease assays were performed using purified proteins incubated with 0.5 M EDTA and subsequently subjected to size exclusion chromatography in SEC buffer (HEPES at pH 8, 200 mM NaCl, 20 mM KCl). Degradation assays were performed in reactions containing 1 µM DNA/RNA substrate and 2 µM protein in reaction buffer (20 mM Tris–HCl, at pH 8.0, 50 mM KCl, 10 mM $MnCl_2$, 2 mM DTT). The reactions were started by adding the protein to the RNA/DNA-containing buffer and then incubated at 37°C for 30 min (exceptions for kinetic assays are indicated). The reactions were stopped by adding 10 µl of SDS-containing loading dye. Afterward, the reaction products were separated in a 20% denaturing urea polyacrylamide gel. The gel was imaged using the ChemiDoc Touch Imaging System equipped with a white light tray (Bio-Rad).

Mass photometry

Mass photometry (MP) analysis was performed using a TwoMP mass photometer (Refeyn Ltd, UK). The instrument was operated with the AcquireMP v2023 R1.1 software (Refeyn Ltd, UK). Microscope coverslips (22 mm × 50 mm, No. 1.5, Marienfeld) and CultureWell Reusable Gaskets (CW-50R-1.0, 3 mm × 1 mm; Grace Bio-labs, USA) were cleaned three times with isopropanol and ultrapure-grade water (Milli-Q, Merck, Germany), air-dried with a compressed air stream, assembled, and mounted with immersion oil (Immersol™ 518F; Carl Zeiss, Germany). For one MP measurement, a drop of 17.5 or 18.5 µl of Tris buffer (20 mM Tris–HCl, at pH 8, 200 mM NaCl, 20 mM $MgCl_2$, 10 mM KCl) or HEPES buffer (25 mM HEPES, at pH 8, 200 mM NaCl, 20 mM $MgCl_2$, 10 mM KCl) was applied to one well of the gasket and focused via the "Droplet dilution" option. Prior to each measurement, protein solutions were freshly pre-diluted to a concentration of 500 nM with either Tris buffer for non-dialyzed protein samples or HEPES buffer for samples dialyzed against HEPES buffer containing $MgCl_2$, which was also used for DNA-binding studies. For the MP measurements, 1.5–2.5 µl of pre-diluted protein mixture was applied to the drop to measure at a final concentration of 37.5–62.5 nM. The volume of applied protein mixture was varied between measurement series to record at an optimal range of particle counts but kept constant across tested samples during each measurement series. For protein–DNA measurements, the 500 nM protein dilutions were pre-incubated with a four-fold molar excess of DNA in HEPES buffer for at least 30 min at room temperature. The MP instrument was calibrated with a custom molecular weight standard (84–336 kDa) that was pre-diluted with either Tris buffer or HEPES buffer, depending on the sample that was measured. MP measurements were recorded for 60 s at 100 frames per second and analyzed with the DiscoverMP v2023 R.1.2 software (Refeyn Ltd, UK). Peaks were fitted with a Gaussian fit, and the total number of counts was predicted by the Gaussian model.

Biolayer interferometry

Biolayer interferometry (BLI) analyses were performed using a BLI(tz) system (ForteBio, Pall Life Science), equipped with high-precision streptavidin (Octet SAX2) biosensors (Satorius, USA) that were derivatized with custom-synthesized biotinylated DNA or RNA fragments (50 nM). Reactions were carried out in buffer containing 25 mM HEPES at pH 8, 200 mM NaCl, 0.05% (v/v) Tween 20, and either 20 mM $MgCl_2$ or $MnCl_2$, as indicated in the figure legends. After the immobilization of the indicated oligonucleotide and the establishment of a baseline, the association behavior of 500 nM YhaM was monitored. After the association phase, the sensor was transferred to a protein-free buffer to follow the dissociation of YhaM. To analyze the interaction of YhaM with single-biotinylated dsDNA (40 bp), two complementary oligonucleotides were incubated at 95°C for 5 min and then annealed by gradual reduction of the temperature. To analyze the interaction of pre-assembled YhaM hexamers with different DNA species, the protein was incubated with ssDNA fragments (2 μM) in buffer containing Mn^{2+} for at least 30 min prior to the experiment. Data were recorded with BLItz Pro 1.2.1.5 software (ForteBio, Pall Life Science) and analyzed using Excel 2019 (Microsoft).

Microscale thermophoresis

The equilibrium dissociation constant for the interaction of YhaM with ssDNA (oligonucleotide listed in Supplementary Table S6) was determined by microscale thermophoresis (MST), using a Monolith NT.115 instrument and NTControl software (v2.1.33) (NanoTemper Technologies GmbH, Germany). Prior to the experiment, YhaM-His_6 was fluorescently labeled using the Monolith His-Tag Labeling Kit RED-tris-NTA 2nd Gen (NanoTemper Technologies GmbH, Germany) as recommended by the manufacturer. A final concentration of 250 nM protein and 50 nM RED-tris-NTA dye was used. ssDNA final concentrations ranging from 8.5 nM to 280 μM, was mixed with the protein-dye solution and subsequently incubated for 15 min prior to the measurement. Experiments were performed at 25°C in buffer containing 25 mM HEPES/NaOH (pH 8), 200 mM NaCl, 0.05% (v/v) Tween 20, and 20 mM $MgCl_2$ using Monolith NT Premium Capillaries (NanoTemper Technologies GmbH, Germany). MST measurements were conducted with the red LED laser, adjusted to a power of 100%, and the infrared laser set to 20% (low). Each experiment was repeated three times independently. Data were analyzed using MO Affinity Analysis v2.3 (Nano-Temper Technologies GmbH, Germany). For curve fitting, the following regions were used for data analysis: cold region from −1 to 0 s and hot region from 1.5 to 2.5 s.

Growth curves

B. subtilis cells were grown to exponential phase, diluted with fresh medium to an optical density at 600 nm (OD_{600}) of 0.01, and transferred into 24-well polystyrene microtiter plates. Growth was monitored by measuring the OD_{600} at 10-min intervals, with three replicates per strain, in an EPOCH2 microplate reader (BioTek®, Germany).

Fluorescence microscopy

Exponentially growing cells cultivated in LB medium at 37°C and 200 rpm were transferred onto 1% agarose pads. Images were taken with an Axio Observer.Z1 (Zeiss) microscope equipped with a Plan Apochromat 100×/1.4 Oil Ph3 phase contrast objective and a pco.edge 3.1 sCMOS camera (PCO). An X-Cite 120PC metal halide light source (EXFO, Canada) and ET-DAPI, ET-YFP, or ET-TexasRed filter cubes (Chroma, USA) were used for fluorescence detection. Nucleoids were visualized by incubating cells with 0.5 μg/ml 4′,6-diamidino-2-phenylindole (DAPI) for 5 min prior to analysis. Images were recorded with VisiView 3.3.0.6 (Visitron Systems, Germany) and processed with Fiji [26].

Spot titer assay

B. subtilis strains were grown on an LB agar plate at 37°C overnight and a single colony was used to inoculate a liquid LB culture. The cultures were grown at 37°C to an OD_{600} between 0.5 and 0.7 and cultures were normalized to an OD_{600} of 0.6. For each stock suspension, serial 10-fold dilutions were prepared by transferring 100 μl samples into 900 μl of sterile LB. The spot-titer assay involved spotting 3 μl samples of each dilution with a calibrated Rainin LTS 20 pipette onto selective media plates containing 30 ng/μl mitomycin C (MMC) or 15 mg/ml 6-(*p*-hydroxyphenylazo)-uracil (HPUra) or exposed to UV light (60 J/m^2). Plates were grown at 30°C overnight.

Quantitative transformation efficiency assay

B. subtilis PY79 [27] freshly restreaked on LB agar plates were transferred to 2 ml LB medium supplemented with inducing agents and antibiotics and grown overnight at 37°C and 200 rpm. The following day, the culture was diluted to an OD_{600} of 0.03 in MC competence medium (10.7 g/l K_2HPO_4, 5.2 g/l KH_2PO_4, 20 g/l dextrose anhydrous (glucose), 22 mg/l ferric ammonium citrate, 1 g/l casein hydrolysate EDM, and 2.2 g/l potassium glutamate monohydrate) and grown at 200 rpm at 37°C until it reached an OD_{600} of 0.5. For transformation frequency assays, 0.5 ml of competent cells were mixed with 0.5 μg of chromosomal DNA (BKE24730 Δ*comGA::erm trpC2* (BGSC [19])) or self-replicative plasmid (pMarB (ECE192 [28])), and incubated for 1 h at 37°C and 200 rpm. Finally, 10^{-1}, 10^{-2}, and 10^{-3} dilutions were plated on LB agar plates with appropriate antibiotics to obtain colony-forming units (CFU). A 10^{-6} dilution was used to determine the number of viable cells. The transformation efficiency was calculated by dividing the total CFU/ml by the number of transformants/ml/μg DNA. For each strain, a technical and biological replicate was performed. Data were visualized using GraphPad Prism 6 (GraphPad Software, San Diego, CA, USA). Transformants were obtained after incubation for 48 h at 30°C [29]. Significance was determined with the Holm–Šídák multiple comparison test using GraphPad Prism version 8.0.1 for Windows (GraphPad Software, Boston, MA, USA).

Results

The deletion of YhaM leads to a drastic reduction in transformability

During our analysis of a *yhaM* deletion strain, we observed a considerable reduction in transformability. To systematically investigate this phenomenon, we performed transformation and transduction assays (Fig. 1). Transformation efficiency was quantified using gDNA that contained an erythromycin resistance cassette flanked by regions for homologous recombination into the *B. subtilis* genome or, alternatively, a self-replicating plasmid also conferring resistance toward the antibiotic erythromycin [28]. In addition, transduction

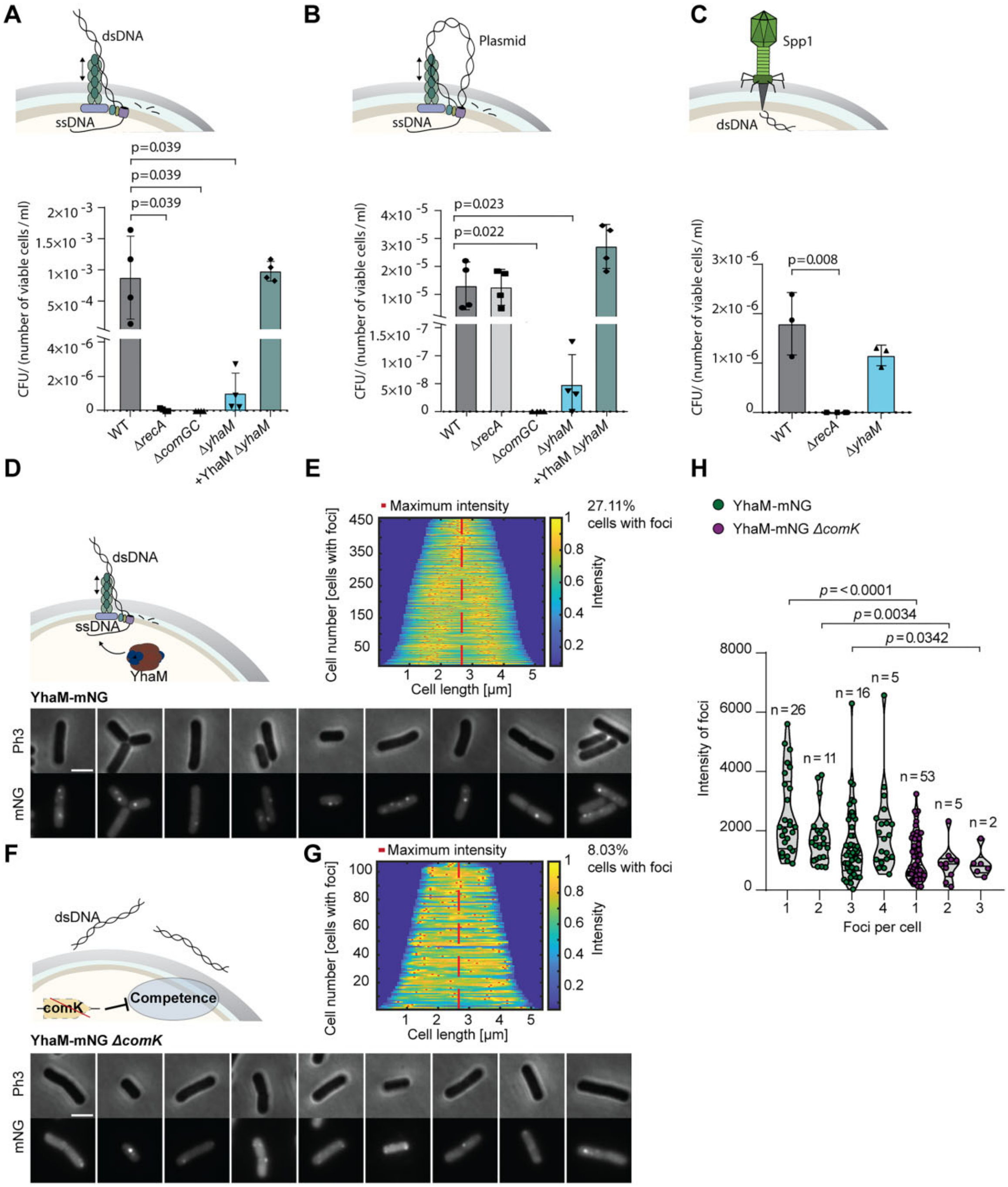

Figure 1. YhaM is required for full competence development. Analysis of the transformation efficiency of *B. subtilis* PY79 and an isogenic *yhaM* mutant (Δ*yhaM*) comparing (**A**) the chromosomal integration of extracellular DNA, (**B**) the uptake of a self-replicative plasmid, and (**C**) phage transduction using the dsDNA phage SPP1. To confirm the strict dependency of chromosomal DNA integration on RecA, a strain lacking RecA (Δ*recA*) was included in the analyses. The dependency of DNA uptake from the environment on type IV-like pili was confirmed using Δ*comGC* cells. To complement the Δ*yhaM* strain, a wild-type copy of *yhaM* was expressed ectopically from the *amyE* site under the control of the hyper-spank promoter. Leaky expression of *yhaM* from the hyper-spank promoter in the absence of the inducer IPTG was sufficient to complement the *yhaM* mutant. The bar charts show the mean values from four independent replicates (dots). Error bars indicate the standard deviation. The transformation efficiency plotted on the *y*-axis was calculated as the ratio of erythromycin-resistant transformants to total colony-forming units. The significance level was calculated using the Holm–Šídák method, using $\alpha = 0.05$ and a *t*-test. *p*-values are indicated. (**D**) Localization of YhaM-mNG in wild-type ($n = 1701$) *B. subtilis* cells grown in competence-inducing conditions 30 min after addition of 0.1 μg/ml gDNA. Shown are representative phase contrast (Ph3) and fluorescence (mNG) images from three independent experiments. Bar: 2 μm. (**E**) Demographic analysis of YhaM-mNG localization in wild-type cells showing YhaM-mNG foci. (**F**, **G**) As described for panels (D) and (E), but for Δ*comK* ($n = 1333$). The relative fluorescence intensity is shown as a heat map with red dots indicating the area of highest intensity in each cell. The color code is given on the right. Cells are aligned at the cell center and sorted by cell length. The total number of cells analyzed for each strain and the percentage of cells showing foci are given for each strain. (**H**) Quantification of number and fluorescence intensity of YhaM-mNG foci per cell for wild-type (green) and Δ*comK* (purple) cells. Each focus is represented by a dot, and the *n* indicates the number of cells analyzed. The fluorescence intensity of foci plotted on the *y*-axis was calculated as the difference between the focus fluorescence and the mean fluorescence of the cell body. The significance levels for the differences in fluorescence intensity were calculated with the Welch's *t*-test, and the corresponding *p*-values are indicated.

susceptibility was evaluated using the *B. subtilis* SPP1 phage to introduce a dsDNA molecule. The incorporation of extracellular gDNA and phage-injected DNA into the recipient genome relies on homologous recombination mediated by the RecA protein [3]. While the SPP1 phage directly injects dsDNA into the cytosol of the host during transduction, transformation with either gDNA or a self-replicating plasmid involves ssDNA intermediates generated during DNA uptake [30, 31]. In addition, transformation with extracellular DNA or plasmid DNA critically depends on a type IV pilus structure on the cell surface, encoded by the *comGC* gene, which is expressed during natural competence, a phenotype triggered by amino acid starvation [4]. Therefore, we included *recA* and *comGC* deletion strains in our DNA uptake assays to assess the relevance of RecA and/or ComGC in the three different DNA transfer mechanisms.

We observed that deletion of the *yhaM* gene resulted in a drastic decrease in transformability for both gDNA and a self-replicative plasmid (Fig. 1A and B). In contrast, transduction with phage SPP1 resulted in a high number of transduced cells, even in the absence of *yhaM* (Fig. 1C). Complementation of the *yhaM* mutant fully restored transformation efficiency to the wild-type level, for both gDNA and the self-replicating plasmid. Plasmid and gDNA uptake via the ComGC pilus structure proceeds via an ssDNA intermediate, while the phage directly injects dsDNA into the host cytosol. Consequently, our findings indicate that the function of YhaM is related to the presence of ssDNA. Additionally, they also suggest that YhaM can function independently of RecA, as the *recA* mutant retains its transformability with plasmid DNA.

To gain further evidence that YhaM function is linked to competence, we investigated the subcellular localization of YhaM. To this end, we replaced the native *yhaM* gene with an allele encoding a derivative of YhaM fused to the fluorescent protein mNeonGreen (YhaM-mNG) in both wild-type cells and an isogenic *comK* deletion background. Deletion of the competence transcription factor *comK* results in a complete loss of competence [32]. The resulting strains were grown in a competence-promoting medium supplemented with gDNA and analyzed microscopically for the localization of YhaM-mNG. In both cases, we observed diffuse fluorescence throughout the cytosol as well as clear fluorescent foci, suggesting that YhaM-mNG condenses at distinct subcellular sites (Fig. 1D and F). Quantification of the YhaM-mNG signal revealed that wild-type cells showed both a higher proportion of cells with foci and a larger number of foci per cell when compared to Δ*comK* cells (Fig. 1E and G and Supplementary Fig. S3). In the *comK* mutant, only 11% of the cells had more than one focus compared to 55% of the wild-type cells. Thirty-six percent of the wild-type cells had more than two foci compared to 3% in the *comK* mutant (Fig. 1D and F). Additionally, the average integrated fluorescence intensity of foci was significantly higher in the presence of ComK than in its absence (Fig. 1H). Despite these differences in the number and intensity of foci, the overall localization pattern of YhaM-mNG appeared to be similar in both strains (Fig. 1D and F). These observations suggest that the formation of YhaM-mNG foci is enhanced in the presence of ComK, providing further support for the involvement of YhaM in natural competence.

Since the *yhaM* gene is controlled by LexA, the master regulator of the SOS response in *B. subtilis*, we also analyzed the sensitivity of a *yhaM* mutant toward DNA-damaging agents [33]. We did not detect an increased sensitivity to DNA damage induced by mitomycin C (MMC), ultraviolet radiation (UV), or 6-(*p*-hydroxyphenylazo)-uracil (HPUra) in the *yhaM* deletion strain, suggesting that YhaM does not have a prominent role in the SOS response of *B. subtilis* (Supplementary Fig. S1). So far, our data suggest that YhaM is critical for successful DNA uptake and consequently might play an important role in the natural competence of *B. subtilis*. As the underlying mechanism still remains unclear, we sought to shed light on the function of YhaM by testing whether it has a so far unappreciated DNA-specific nuclease activity involved in the processing of DNA after uptake.

YhaM is a 3′-deoxyribonuclease specific for ssDNA

DNA taken up during competence enters the cytoplasm in the single-stranded state in 3′–5′ direction [6]. YhaM, a nuclease conserved among Gram-positive bacteria (Supplementary Table S1), has previously been reported to exhibit RNA-specific 3′–5′ exoribonuclease activity [15, 16, 34]. So far, the functions of YhaM or homologs such as Cbm (*Streptococcus pyogenes*), SAOUHSC_01973 (*S. aureus*), and CA_C2261 (*Clostridium acetobutylicum*) have only been linked to 3′ processing in diverse RNA degradation/modification pathways, but only with minor influence on the fitness of the host organisms [35]. A connection between the YhaM homolog Cbf1 from *S. pneumoniae* and natural competence has been established based on the finding that Cbf1 has a role in stabilizing small regulatory RNAs (sRNAs), promoting their function as negative regulators of competence, although the precise mechanism is not fully understood [34].

Our findings point to an involvement of YhaM in natural competence, suggesting that it may have a different activity than the previously reported RNase activity [15, 36]. To test this hypothesis, we determined the ability of YhaM to bind different types of nucleic acids using BLI (Fig. 2A). To this end, comparable amounts of ssDNA, dsDNA, or single-stranded RNA (ssRNA) oligonucleotides were immobilized on a biosensor and probed with purified YhaM (Fig. 2A, Supplementary Fig. S4). The results obtained indicate that YhaM binds most strongly to ssDNA, as evidenced by the highest wavelength shift, while its interaction with either dsDNA or ssRNA is significantly weaker. The affinity of YhaM for dsDNA and ssRNA is similar, suggesting that these species may be off-targets for YhaM. MST experiments confirmed that YhaM strongly binds ssDNA with an equilibrium dissociation constant of 500 nM (Fig. 2B).

Nuclease assays using 5′-6-carboxyfluorescein (FAM)-labeled 40-nt ssDNA and ssRNA molecules as substrates demonstrated that YhaM degrades both ssDNA and ssRNA with high efficiency (Fig. 2C and E). Consistent with previous findings, the nuclease activity of YhaM was strictly dependent on Mn^{2+} and was inhibited in the presence of Mg^{2+} (Supplementary Fig. S5) [15]. While ssDNA was degraded, no cleavage of dsDNA was observed when a 5′-FAM-labeled 23-nt dsDNA molecule was used as a substrate, indicating a specificity of YhaM for ssDNA regions (Fig. 2D). Whereas ssDNA 3′ overhangs of varying lengths (36 or 21 nt) were efficiently degraded, 5′ overhangs remained intact (Fig. 2D and F and Supplementary Fig. S6), thus identifying YhaM as a 3′-deoxyribonuclease.

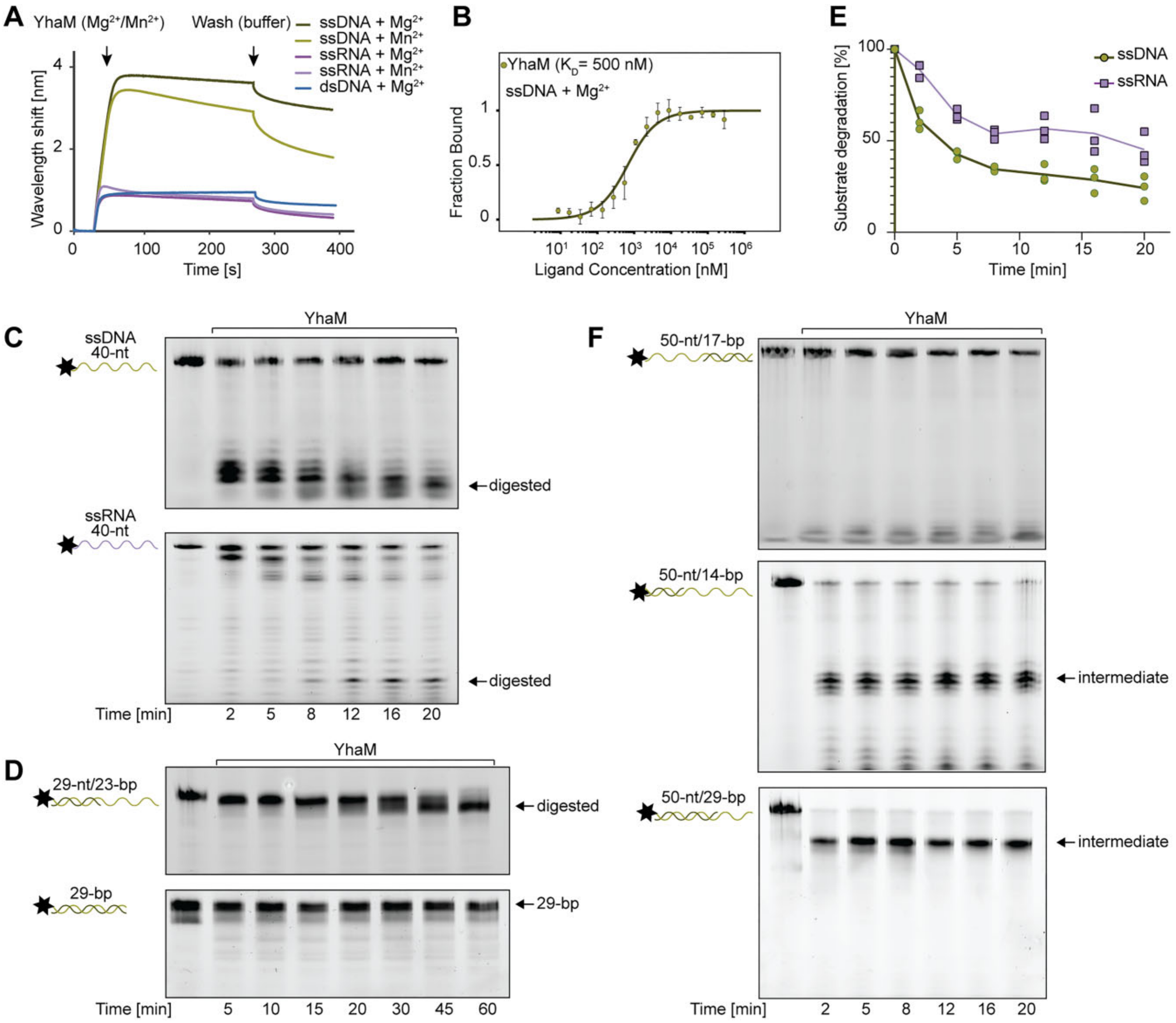

Figure 2. YhaM shows a strong preference for ssDNA over dsDNA and ssRNA. (**A**) BLI analysis investigating the interaction of YhaM with ssDNA, dsDNA, and ssRNA in the presence of the indicated divalent cations. Depicted is a representative measurement from three independent experiments. (**B**) MST analysis of the affinity of YhaM for ssDNA. The equilibrium dissociation constant ($K_D = 500$ nM) was calculated from three independent experiments. Error bars indicate the standard deviation. (**C**, **D**, **F**) 20% of urea PAGE gels showing the digestion kinetics of (**C**) ssDNA and ssRNA and (**D**, **F**) ssDNA/dsDNA hybrids with varying accessibility of single-stranded 3′-end DNA. For the ssDNA/dsDNA hybrids, the total length of the hybrids in nucleotides (nt) and the lengths of their dsDNA region (bp) are indicated. The star indicates the 5′ attachment site of the 6-carboxyfluorescein label. Nucleic acids were always digested in the presence of Mn^{2+} (10 mM). (**E**) YhaM-dependent ssRNA (violet) and ssDNA (green) degradation as quantified from gels shown in panel (A). Shown are the values obtained in three independent experiments.

YhaM forms a hexamer in solution

Size exclusion chromatography showed that YhaM (∼35 kDa) eluted as a complex with a molecular weight of ∼210 kDa, corresponding to a hexamer (Supplementary Fig. S4). To determine how this complex forms, we analyzed the molecular weight distribution of purified YhaM by MP. To study substrate binding and assembly without the potential artifacts from substrate degradation, we utilized buffers containing Mg^{2+}, which produce an enzymatically inactive enzyme (Supplementary Fig. S5). At nanomolar concentrations, the predominant oligomeric species of YhaM in solution were hexamers (Fig. 3A and B). After treatment with EDTA, a chelating agent that binds divalent metal ions, the proportion of YhaM hexamers decreased drastically. At the same time, two other species were formed, corresponding to YhaM dimers and tetramers. Dialysis of the EDTA-treated YhaM sample against Mg^{2+}-containing buffer was insufficient to completely restore the hexameric form of YhaM. However, dialyzed YhaM almost fully reverted back to the hexameric state when it was incubated with a four-fold molar excess of ssDNA (Fig. 3A and B), demonstrating that ssDNA and divalent cations are required to achieve efficient YhaM hexamer formation (Fig. 3B).

The results obtained suggest that YhaM accumulates around its ssDNA substrate gradually. To test this hypothesis, we analyzed the effect of the oligomeric state of YhaM on its DNA binding efficiency. To this end, ssDNA loops or dsDNA fragments were immobilized as substrates on biosensors and probed with YhaM dimers or hexamers. In direct comparison, pre-assembled hexameric YhaM exhibited weaker binding to

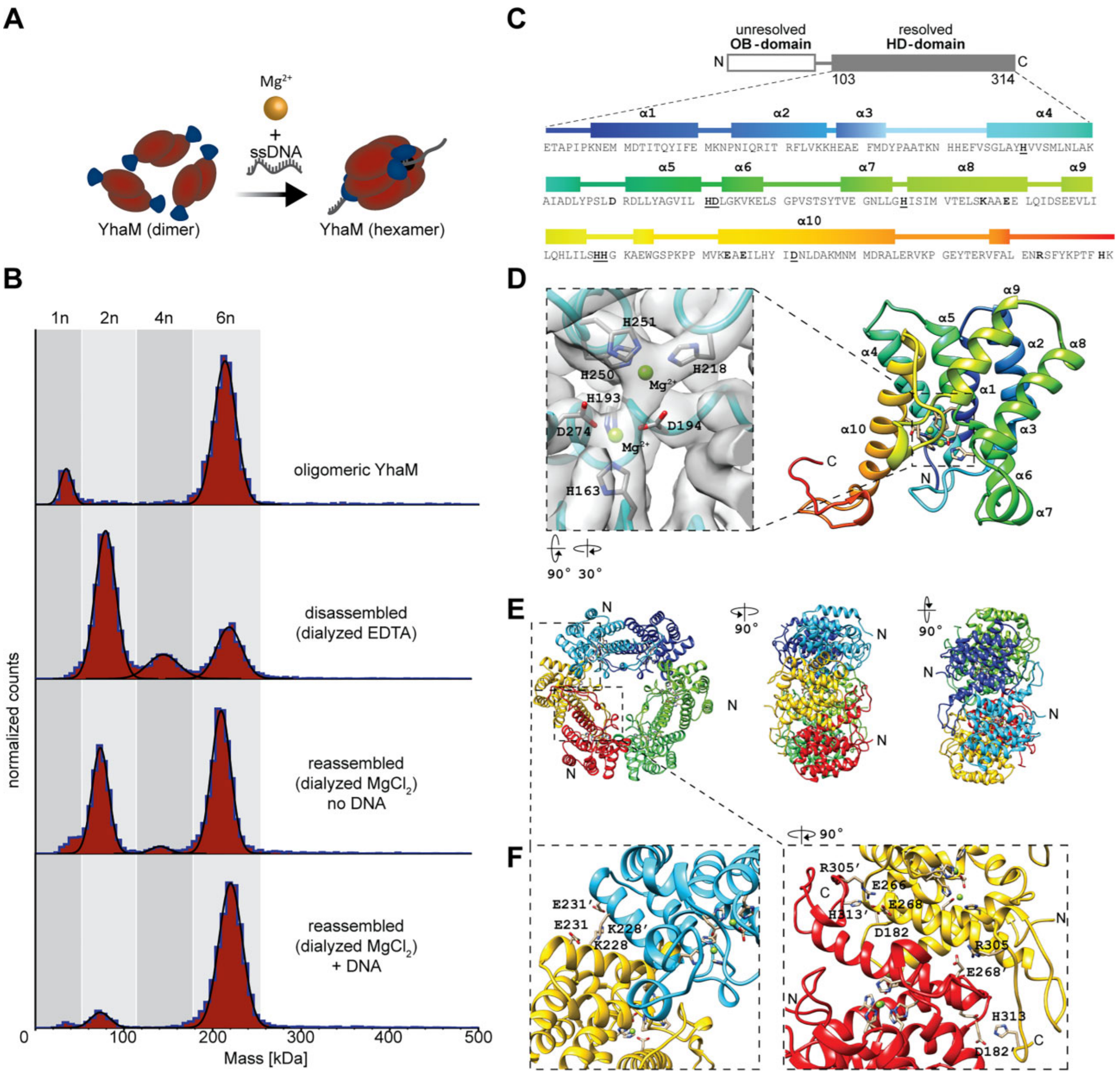

Figure 3. Structural characterization of YhaM by cryo-EM. (**A**) Model of the process of YhaM assembly. (**B**) MP analysis of the oligomerization state of YhaM. The estimated molecular weights of the different YhaM species observed are 35 kDa (monomer), 70 kDa (dimer), 140 kDa (tetramer), and 210 kDa (hexamer). (**C**) Schematic showing the domain organization of YhaM, with the HD domain resolved by cryo-EM highlighted in gray. The amino acid sequence of the YhaM HD domain is shown, with secondary structural elements depicted schematically above the sequence, colored in a rainbow gradient from N- to C-terminus. The active site residues are underlined and highlighted in bold, while the residues involved in salt bridge formation during YhaM oligomerization are also shown in bold only. (**D**) Cartoon representation of a YhaM monomer, colored in a rainbow gradient from N- to C-terminus (denoted by "N" and "C," respectively; PDB ID: 9H3F). Active site residues are depicted as sticks, while coordinated magnesium ions are shown as spheres. A magnified view of the active site highlights amino acids of the extended H…HD…HH…D motif, along with the two coordinated magnesium ions. Cryo-EM map densities (EMD-51819) at a 3σ contour level are displayed in transparent gray for the active site region. (**E**) Top-down and side views of the YhaM hexamer, illustrating its D3 symmetry. Individual monomers are color-coded. N-termini (denoted by "N") oriented outward from the image plane are indicated. In the top-down view, one example of each of the two distinct interaction surfaces formed by D3 symmetry is shaded in gray. (**F**) Magnified views of the contact interfaces between two YhaM subunits, with residues contributing to salt bridge formation being indicated. Further details are provided in the main text.

both substrates, as indicated by a lower wavelength shift. In contrast, YhaM dimers showed a significantly stronger wavelength shift when incubated with either of the DNA substrates (Supplementary Fig. S7). Since the presence of Mg^{2+} promotes hexamer formation (Fig. 3B), one possible explanation for this observation is that YhaM reassembles into hexamers around both ssDNA and dsDNA molecules. This interpretation aligns with the finding that both Mg^{2+} and DNA are required to fully restore YhaM hexamers from EDTA-dissociated dimers (Fig. 3B).

In silico analysis of YhaM revealed the presence of an N-terminal oligonucleotide-binding (OB) domain (amino acids 20–90), typically associated with nucleic acid binding and recognition, and a C-terminal histidine/aspartate (HD) domain (amino acids 163–279), which contains the catalytic residues required for nucleic acid cleavage (Fig. 3C). To obtain more insights into the arrangement of YhaM subunits and their different domains in the hexameric complex, we determined the molecular structure of YhaM by cryo-EM.

Our cryo-EM analysis revealed that YhaM indeed adopts a hexameric ring structure with a dihedral symmetry of order 3 (D3) (Fig. 3E and F and Supplementary Fig. S8). Notably, only the C-terminal residues 103–314, which correspond to the HD domain, yielded interpretable density maps, with the local resolution ranging from 2.9 to 3.1 Å, allowing the reconstruction of the HD domain (Fig. 3D). In contrast, the N-terminal OB domain exhibited no clear densities, likely due to significant flexibility, and was therefore unresolved in the structure.

A reduction in resolution was observed near the surface of the hexameric ring, which we attribute to the highly dynamic nature of the OB domain (Supplementary Figs S8 and S9 and Supplementary Table S2). Structural modeling using AlphaFold3 [23] predicts that the OB domains extend above and below the plane of the hexameric ring, and are connected to the HD domain by a flexible linker region, which may contribute to the decreased resolution (Fig. 4A). Despite these limitations, the resolution within the HD domain was sufficient to precisely localize two magnesium ions coordinated by an extended HD motif (H163, H193, D194, H250, H251, and D274) at the active site of the hydrolase (Fig. 3D), placing YhaM in the family of diphosphatases, which also include YqeK (an Ap4A hydrolase), YpgQ (a member of the RNase Y family), and SpoT (a hydrolase of the alarmone (p)ppGpp) [37–39].

Coordination of divalent cations by the HD motif is essential for YhaM oligomerization

The absence of YhaM results in a significant reduction in transformability (Fig. 1). Both our binding and nuclease experiments demonstrated that YhaM strongly binds and efficiently degrades ssDNA (Fig. 2). These findings support the hypothesis that YhaM plays a crucial role in ssDNA processing rather than functioning mainly as a ribonuclease, as previously assumed [35]. To investigate the involvement of YhaM in DNA uptake, we aimed to understand whether the OB domain and the HD domain independently contribute to YhaM oligomerization and DNA binding and, therefore, to the potential processing of incoming ssDNA.

To this end, we introduced amino acid substitutions in both domains and analyzed the oligomerization properties of the mutant proteins by MP and BLI (Fig. 4).

First, we generated YhaM variants in which tryptophan 51 (W51A) or tyrosine 76 (Y76A) in the OB domain was replaced by alanine. Residues W51 and Y76 are highly conserved across OB domains and have previously been shown to contribute to nucleic acid binding [15]. In addition, we introduced two amino acid exchanges (H193A D194A) in the HD motif of the HD domain to remove hydrolytic activity and produce an enzymatically inactive variant [40]. MP experiments revealed a similar assembly pattern for the W51A and Y76A variants as for the wild-type protein (Fig. 4B). A predominant hexameric species (70%) was observed for the W51A variant. Upon treatment with EDTA, the proportion of hexameric species decreased to 19%, accompanied by a significant increase in the dimeric population. Addition of Mg^{2+} partially shifted the dimeric YhaM population back to the hexameric form. $YhaM^{Y76A}$ displayed a similar behavior to the W51A variant. Further analyses showed that, as for the wild-type protein, the addition of ssDNA was required to fully restore the hexameric state of $YhaM^{Y76A}$. Taken together, the oligomerization properties of the two variants with defects in the OB domain resembled those of the wild-type protein. In sharp contrast, the variant featuring the mutant HD domain ($YhaM^{H193A/D194A}$) was almost exclusively detected as a dimeric species. The addition of EDTA or Mg^{2+} did not induce the formation of monomeric or hexameric species, respectively. However, adding ssDNA resulted in a slight increase in the tetrameric and hexameric YhaM population, supporting a possible role of nucleic acids in YhaM oligomerization. The results of the MP analysis suggest that the coordination of divalent cations is essential for YhaM hexamer formation and, as already suggested by our structural data, can occur independently of the OB domain.

Next, we determined whether amino acid exchanges in either the OB domain or the HD domain influence ssDNA binding, using BLI (Fig. 4C). $YhaM^{Y76A}$ shows a drastically reduced interaction with ssDNA when compared to the wild-type protein. In contrast, mutation of the HD motif resulted in stronger binding to the ssDNA substrate. Both YhaM variants only showed poor binding to ssRNA (Fig. 4C). This illustrates the importance of the domains in substrate binding. The enzyme's function is reliant on both substrate binding and enzymatic activity, as well as the resulting oligomerization (Fig. 4D).

YhaM acts on chromosomal DNA *in vivo*

YhaM was identified as a 3′-deoxyribonuclease essential for DNA uptake during natural competence (Fig. 1). Our *in vitro* data clearly demonstrate that YhaM preferentially binds and degrades ssDNA (Fig. 2). However, to rule out the possibility that our *in vivo* observations in *B. subtilis* were influenced by RNA-related processes, we considered previous findings by Hör *et al.* showing that YhaM affects competence in *S. pneumoniae* by stabilizing ssRNA through trimming of a few nucleotides [34]. To further support our hypothesis that YhaM primarily interacts with DNA, we constructed *B. subtilis* strains expressing the genes for $YhaM^{W51A}$, $YhaM^{Y76A}$, or $YhaM^{H193A/D194A}$ under the control of the IPTG-inducible $P_{hyper\text{-}spank}$ promoter from the *amyE* locus [20] in a Δ*yhaM* background.

First, we explored the effect of the overproduction of the different YhaM variants on cell growth. While the wild-type strain and the *yhaM* deletion mutant showed a similar growth behavior, the strain expressing the inducible wild-type copy of *yhaM* showed a marked decrease in the final optical density of the culture. We tested whether increased unspecific RNase activity could be the reason for this growth defect. However, a control strain overproducing RNase PH from the same promoter and locus showed no growth defect (Fig. 5A) [41]. No decrease in the optical density of the culture was observed for strains overproducing the OB domain variants $YhaM^{W51A}$ and $YhaM^{Y76A}$, which both showed reduced DNA-binding activity in the BLI analysis (Fig. 4C). Complete lysis was observed for a strain producing the catalytically inactive $YhaM^{H193A/D194A}$ variant, which is impaired in

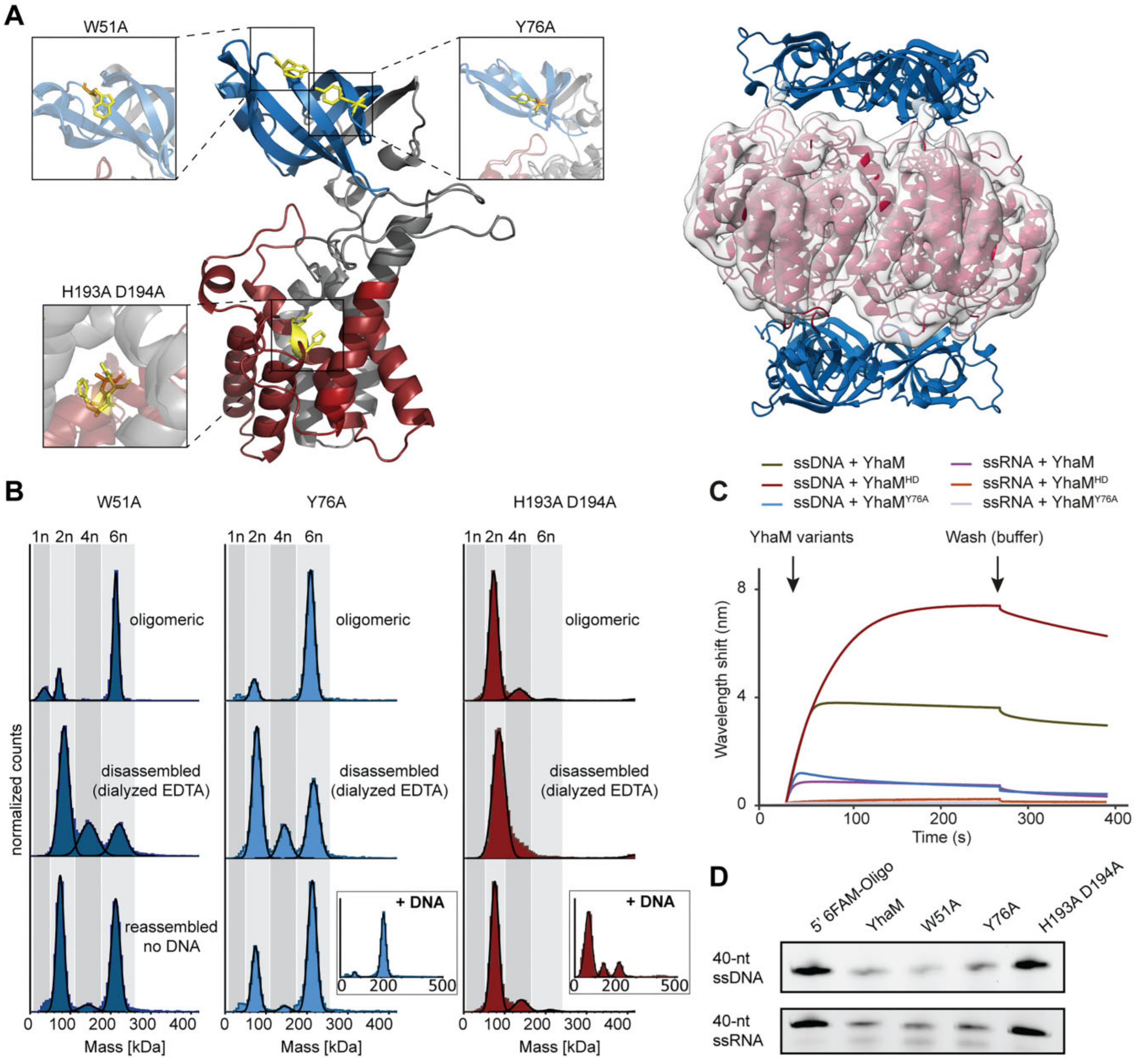

Figure 4. Histidine/aspartic acid coordination of divalent cation enables YhaM oligomerization. (**A**) Reconstructed volume of YhaM, rendered at a low contour level, with fitted AlphaFold3 model (cartoon). The N-terminal OB-fold domain is shown in blue, and the hydrolase domain (HD) is shown in red. The AlphaFold3 model of a YhaM monomer at the right side shows the positions and names of the amino acid residues exchanged in the mutant proteins. (**B**) Analysis of the oligomeric state of mutant YhaM proteins by MP. MP shows that hexamer formation for YhaM^{Y76A} is facilitated by divalent cations and illustrates directed assembly of YhaM using oligonucleotides. The YhaM$^{H193A/D194A}$ almost completely lost its ability to form a hexameric assembly. (**C**) BLI analysis of the binding of YhaM^{Y76A} and YhaM$^{H193A/D194A}$ to ssDNA or ssRNA in the presence of Mg^{2+}. Different oligonucleotides were immobilized on biosensors prior to the loading of YhaM. Three independent experiments were performed, and representative measurements are shown. (**D**) Representative 20% urea PAGE gel showing the digestion kinetics of 5′-FAM-labeled ssDNA and ssRNA.

oligomerization (Figs 4B and 5A) but showed increased binding to ssDNA *in vitro* (Fig. 4C).

To further investigate the phenotype of the different overproduction strains, we performed microscopic analyses of cell morphology and visualized the chromosomes with the fluorescent dye DAPI (Fig. 5B and C). We observed that the overproduction of YhaM and YhaM$^{H193A/D194A}$ resulted in significant chromosome condensation (nucleoid aggregation) and abnormal cell elongation (Fig. 5B and C). Condensed chromosomes appeared as single, small central masses of DNA irregularly distributed within elongated cell bodies, whereas wild-type cells had a regular length with evenly distributed DNA. We did not observe marked changes in cell length or the condensation state of chromosomal DNA in cells overproducing the OB domain variants YhaM^{W51A} and YhaM^{Y76A} or RNase PH. Similarly, no alteration in cell length or nucleoid morphology was observed for the *yhaM* deletion mutant (Fig. 5B and C). We also visualized the localization of DNA by performing a demographic analysis of the DAPI signal (Supplementary Fig. S10) [42]. To provide evidence that chromosome condensation is a consequence of YhaM interacting with DNA, we created a strain that produces fluorescent YhaM-mNG from the native *yhaM* locus in the YhaM-overproducing background. A clear colocalization of YhaM-mNG foci and chromosomal DNA

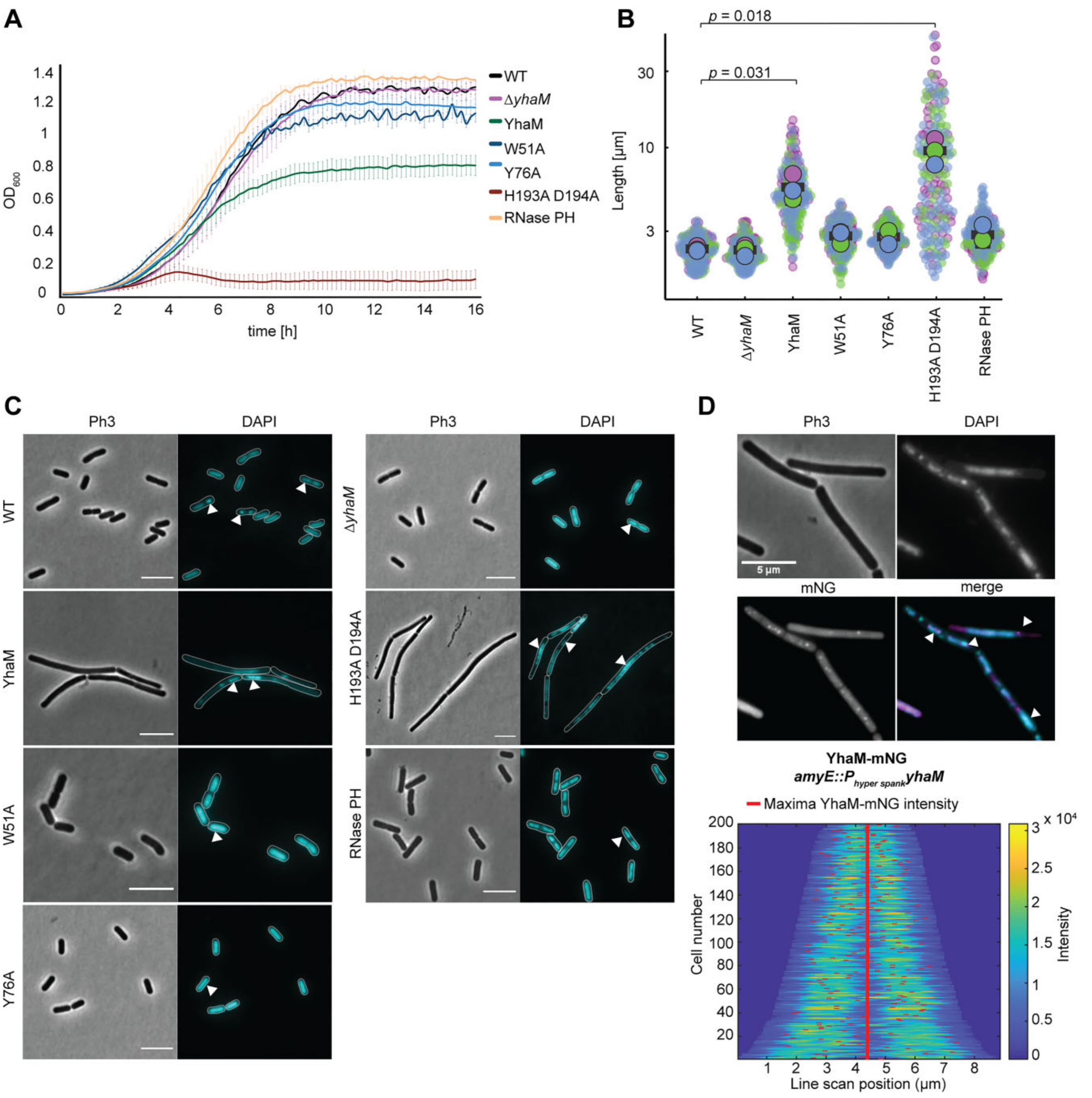

Figure 5. Overproduction of YhaM results in reduced fitness and abnormal cell morphology. (**A**) Growth curves of the strains overproducing YhaM and variants thereof after induction with 1 mM IPTG. A strain producing RNase PH was used as a control. (**B**) Distribution of cell lengths in populations of the *B. subtilis* strains analyzed after 5 h of induction with 1 mM IPTG. Large dots represent the median values of each independent replicate (blue, green, red). Small dots represent the individual data points. *p*-values for significant comparisons (*t*-test) are indicated. (**C**) Localization of DNA by DAPI staining in strains producing YhaM or the indicated YhaM variants after 5 h of induction with 1 mM IPTG. White arrows indicate regions of DNA accumulation. Scale bar: 5 µm. (**D**) Colocalization of DAPI-stained chromosomal DNA and YhaM-mNG in the YhaM overproduction background. Arrowheads indicate the localization of the chromosome visualized by DAPI signal. To generate the demograph on the left, the DAPI fluorescence profiles were stacked vertically according to cell length. The color code is given on the right. Red dots represent the maximum fluorescence intensity of the YhaM-mNG fluorescence channel, indicating the subcellular positions of YhaM-mNG foci. The red line indicates the positions of the cell centers.

was observed in this strain. An analysis of the cellular distribution of YhaM-mNG confirmed that YhaM-mNG foci consistently localized to the DAPI-stained nucleoid or in very close proximity (Fig. 5D), indicating the significant role of YhaM in DNA-related processes. These findings not only support the above *in vitro* data but also highlight the critical importance of the OB domain in the process of substrate recognition, suggesting that the OB domain functions as a key element in the interaction between YhaM and its DNA targets.

YhaM of *S. aureus* complements the *B. subtilis yhaM* phenotype

To gain insights into the conservation of YhaM function in natural competence in other Gram-positive organisms, we chose to functionally analyze the YhaM ortholog of the human pathogen *S. aureus* (*Sa*YhaM). To determine whether *Sa*YhaM also showed ssDNA-binding activity, we cloned the corresponding gene (GenBank accession number: CAA3917979.1), overproduced it in *E. coli*, and analyzed

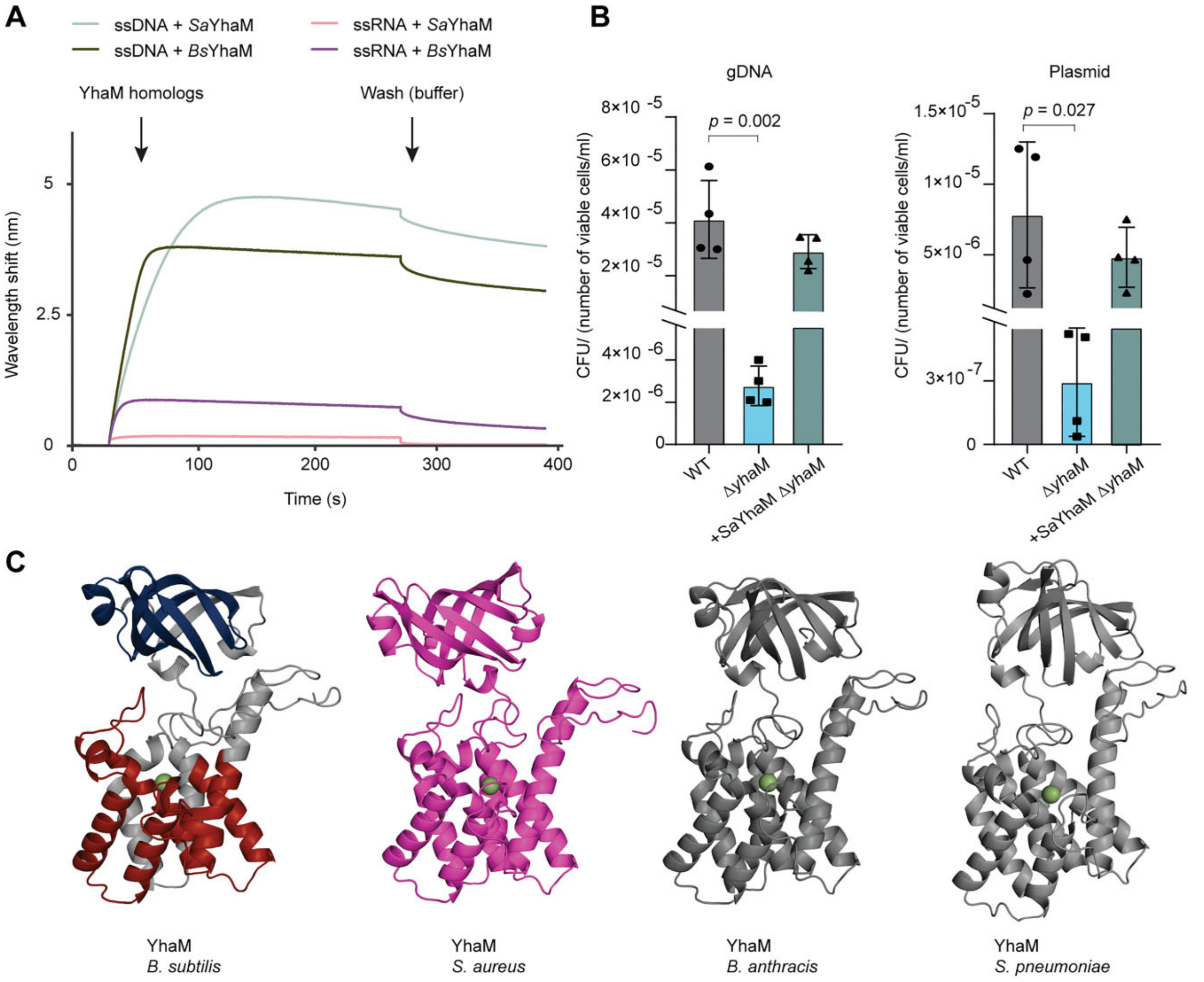

Figure 6. *Sa*YhaM prefers ssDNA and enables ssDNA processing in *B. subtilis*. (**A**) Representative BLI measurement showing the interaction of different YhaM homologs with ssRNA or ssDNA. Oligonucleotides were first immobilized on BLI sensors and then incubated with either *Sa*YhaM or *Bs*YhaM. Experiments were performed three times. (**B**) Transformation efficiency of *B. subtilis* (PY79) during natural competence. The assays were performed with an erythromycin-resistant cassette flanked by homologous regions for recombination into the *B. subtilis* chromosome and a self-replicating plasmid that does not require recombination for its establishment in the cell. Wild-type and *ΔyhaM* cells as well as a strain complemented with the gene encoding *Sa*YhaM were analyzed. Bars represent the mean values of four independent replicates. Error bars indicate the population standard deviation, and dots represent the data of individual measurements. Statistical significance was determined using a *t*-test. *p*-values for significant differences are shown. (**C**) Structural alignment of AlphaFold3 models of *Bs*YhaM, *Sa*YhaM, *Ba*YhaM, and *Sp*YhaM. For *Bs*YhaM, the domain structure is indicated by colors (blue: OD domain; red: HD domain). The green sphere indicates a divalent cation (Mn^{2+}).

the purified protein for its ssDNA- and ssRNA-binding activity using BLI. Like its homolog from *B. subtilis* (*Ba*YhaM), *Sa*YhaM also interacted more strongly with ssDNA than with ssRNA (Fig. 6A). Moreover, size exclusion chromatography showed that it also assembled into a hexameric complex (Supplementary Fig. S11), suggesting that it has a similar biochemical function.

To test whether *Sa*YhaM could substitute *Ba*YhaM, we introduced the *S. aureus* gene into *B. subtilis* to complement the deletion of *yhaM*. We found that *Sa*YhaM was indeed able to fully restore transformability of the mutant strain with both chromosomal and plasmid DNA (Fig. 6B). A structural alignment of AlphaFold3 [23] models of YhaM orthologs from pathogenic representatives such as *S. aureus*, *B. anthracis*, and *S. pneumoniae* demonstrates a high structural similarity of the different proteins (Fig. 6C). Thus, *Sa*YhaM is able to restore competence in *B. subtilis* and conserved in relevant pathogens (Supplementary Table S1), suggesting that YhaM may play a crucial role in DNA uptake in important human pathogens, thereby likely contributing to the spread of antibiotic resistance among clinically relevant strains.

Discussion

Understanding DNA uptake in naturally competent bacteria is crucial for unraveling the mechanisms of HGT, a process that plays a key role in genetic diversity, antibiotic resistance, and bacterial evolution [1, 2].

Despite extensive research, it is unknown how bacteria regulate the processing of incoming ssDNA once it enters the cytosol. While several DNA-binding proteins such as Ssb and recombinases such as RecA are known to protect and

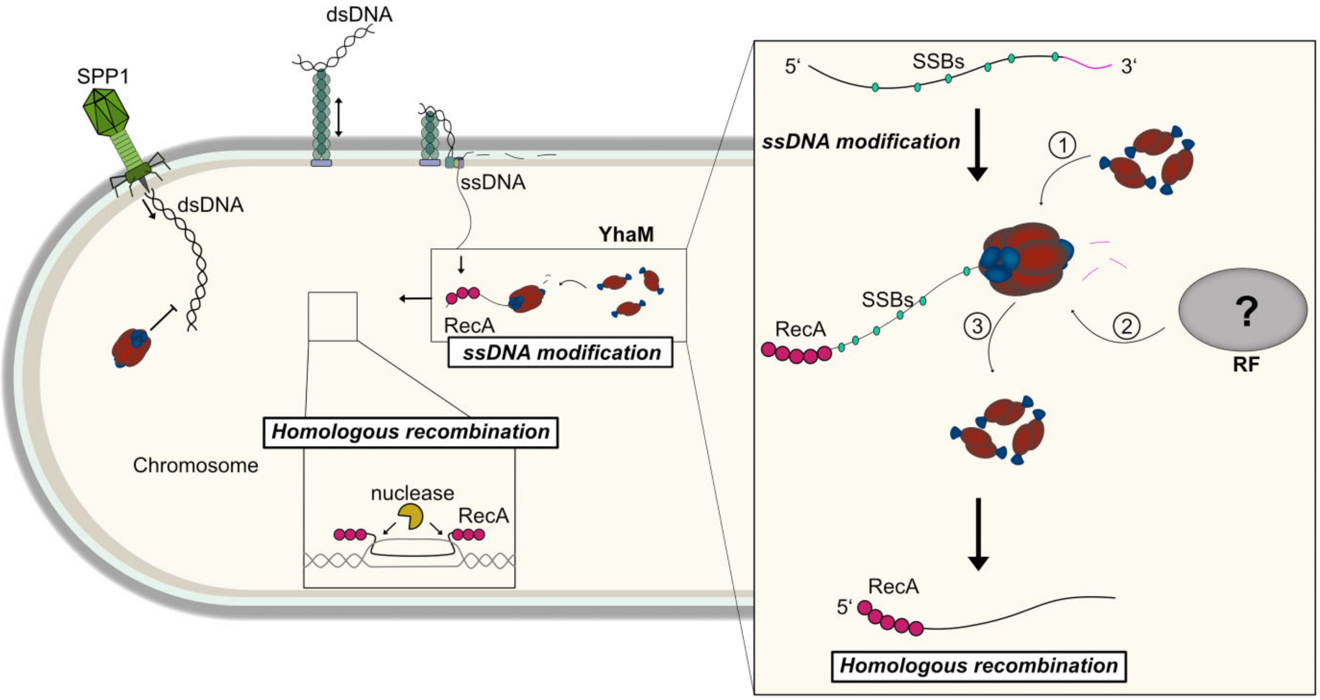

Figure 7. YhaM processes ssDNA after uptake during natural competence in Gram-positive organisms. YhaM plays a crucial role in the competence of bacteria and acts as a gatekeeper for DNA uptake. During natural competence, environmental DNA is taken up by the retraction of a pilus structure into the periplasm. The non-transforming strand will be transferred through a channel protein into the periplasm, while the transforming strand is taken up. After its uptake, ssDNA will be directly bound by single-stranded binding proteins and RecA. RecA is involved in homologous recombination together with an endonuclease. YhaM processes the ssDNA that has entered the cytosol immediately after its uptake, enhancing its 3′ maturation for further integration (1). The maturation process must be regulated by a release factor (2) that controls ssDNA turnover and prevents the complete degradation of the imported ssDNA fragment. The utilization of DNA from the environment is strictly dependent on YhaM (3).

integrate ssDNA, it remains unclear whether additional factors influence ssDNA stability, degradation, or recombination efficiency. In particular, the role of exonucleases in ssDNA processing post-uptake has not been fully explored.

In this study, we present YhaM as a critical ssDNA processing nuclease involved in DNA uptake during natural competence. While the role of YhaM in 23S rRNA maturation has been previously described [43], its involvement in DNA metabolism has remained largely unexplored [35]. Although homologs such as CBF1 in *S. aureus* have been linked to ribosome turnover and 3′ exoribonuclease activity, no direct connection to DNA uptake had been established [16]. Hör *et al.* provided initial evidence of YhaM’s competence-related function, showing its role in stabilizing sRNAs that regulate competence in *S. pneumoniae* [34]. Our findings extend this work by demonstrating that YhaM directly facilitates ssDNA processing after uptake in *B. subtilis*.

Our competence assays reveal that the deletion of *yhaM* significantly impairs the ability to take up DNA, a defect that can be rescued by ectopic expression of YhaM or its ortholog from *S. aureus*, confirming its essential role in ssDNA uptake across different organisms (Figs. 1 and 6). Interestingly, phage-mediated transduction, another type of HGT where dsDNA directly enters the cytosol [44], was unaffected in Δ*yhaM* mutants, suggesting that YhaM specifically facilitates the processing of ssDNA rather than DNA entry itself. Transformation experiments with both chromosomally integrating DNA and non-integrating plasmids further support the idea that YhaM acts immediately after ssDNA entry, functioning independently of homologous recombination (Fig. 1). A potential later effect of YhaM on homologous recombination can be ruled out, as no impact would be expected on a self-replicating plasmid, which follows a RecA-independent process [10].

We eliminate the possibility that our observations are due to RNA-related processes through both biochemical and *in vivo* studies. Structural and biochemical analyses show that YhaM assembles into hexamers in the presence of divalent cations, preferentially binding ssDNA (Figs. 2 and 3). In overproduction studies, YhaM also binds DNA *in vivo*, supporting the hypothesis that its primary function involves DNA processing (Fig. 5). Our data also suggest that YhaM does not carry out this processing in isolation. Considering the degradation assays and the binding assays (Fig. 2), which indicated that YhaM prompts a turnover of the substrate and does not disintegrate without the addition of EDTA, we believe that in a biological context, an interaction partner must instigate the disintegration of the hexameric enzyme. We propose that an unidentified interaction partner may regulate YhaM’s processing of ssDNA and prevent complete degradation of the incorporated DNA.

Although *yhaM* is transcriptionally regulated by LexA, Δ*yhaM* mutants do not exhibit increased DNA damage sensitivity, suggesting that YhaM does not play a significant role in the SOS response itself (Supplementary Fig. S1). However, its involvement in competence highlights a strong functional link between the SOS response and DNA uptake. This connection appears to be context-dependent, as YhaM homologs in different species, such as *S. pneumoniae* and *S. aureus*, exhibit diverse roles in nucleic acid metabolism [15, 16, 34, 45, 46].

We propose a model in which YhaM processes the 3′ end of transforming ssDNA upon entry into the cytosol, ensuring efficient DNA uptake and integration (Fig. 7).

Acknowledgements

We thank Thomas Heimerl for his support during the cryo-EM analysis, Patrik Brück for help with the construction of strains, and Alexandra Kilb, Sebastian Pöhl, Michael Vockenhuber, and Maximilian Greger for helpful discussions.

Author contributions: J.P.-F., J.H., and R.H. conceived the study. M.M. and R.H. constructed plasmids and strains. M.M. and R.H. conducted the *in vitro* experiments. R.H. performed the microscopy studies, growth analyses, biochemical experiments, and transformation/transduction efficiency experiments. M.M. measured the growth curves. J.H. performed BLI and MST experiments and AlphaFold3 modeling. L.F., M.G.M., and J.P.-F. collected and processed the cryo-EM datasets, refined the structures, and analyzed negative-stain EM data, with the guidance provided by C.Z., who also provided the cryo-EM infrastructure. M.G. and F.L.S. performed the mass photometry measurements. J.H., J.P.-F., and R.H. wrote the manuscript, with discussion and input from all other authors. M.T., G.B., G.K.A.H., and M.L. reviewed and edited the manuscript.

Supplementary data

Supplementary data is available at NAR online.

Conflict of interest

None declared.

Funding

This work was funded by the University of Marburg (core funding to M.T.), the Max Planck Society (Max Planck Fellowships to M.T. and G.B.), the European Research Council (grant agreement 101097986—C-SWITCH to M.T.), and the German Research Foundation (project 505997786—GRK 2937 to M.T., G.B., M.L., and R.H.). J.H. acknowledges funding from the International Max Planck Research School for Environmental, Cellular and Molecular Microbiology (IMPRS-Mic). M.G. acknowledges support by a Peter und Traudl Engelhorn-Stiftung postdoctoral fellowship.

Data availability

Coordinates and structure factors have been deposited within the Protein Data Bank (PDB) under the accession code 9H3F and EMD-51819. The authors declares that all other data underlying this article are available in the article and in its online supplementary material.

References

1. Lerminiaux NA, Cameron ADS. Horizontal transfer of antibiotic resistance genes in clinical environments. *Can J Microbiol* 2019;**65**:34–44. https://doi.org/10.1139/cjm-2018-0275
2. Soucy SM, Huang J, Gogarten JP. Horizontal gene transfer: building the web of life. *Nat Rev Genet* 2015;**16**:472–82. https://doi.org/10.1038/nrg3962
3. Dubnau D, Blokesch M. Mechanisms of DNA uptake by naturally competent bacteria. *Annu Rev Genet* 2019;**53**:217–37. https://doi.org/10.1146/annurev-genet-112618-043641
4. Chung YS, Dubnau D. ComC is required for the processing and translocation of comGC, a pilin-like competence protein of *Bacillus subtilis*. *Mol Microbiol* 1995;**15**:543–51. https://doi.org/10.1111/j.1365-2958.1995.tb02267.x
5. Kilb A, Burghard-Schrod M, Holtrup S *et al.* Uptake of environmental DNA in *Bacillus subtilis* occurs all over the cell surface through a dynamic pilus structure. *PLoS Genet* 2023;**19**:e1010696. https://doi.org/10.1371/journal.pgen.1010696
6. Beiter K, Wartha F, Albiger B *et al.* An endonuclease allows *Streptococcus pneumoniae* to escape from neutrophil extracellular traps. *Curr Biol* 2006;**16**:401–7. https://doi.org/10.1016/j.cub.2006.01.056
7. Yadav T, Carrasco B, Myers AR *et al.* Genetic recombination in *Bacillus subtilis*: a division of labor between two single-strand DNA-binding proteins. *Nucleic Acids Res* 2012;**40**:5546–59. https://doi.org/10.1093/nar/gks173
8. Yadav T, Carrasco B, Hejna J *et al.* *Bacillus subtilis* DprA recruits RecA onto single-stranded DNA and mediates annealing of complementary strands coated by SsbB and SsbA. *J Biol Chem* 2013;**288**:22437–50. https://doi.org/10.1074/jbc.M113.478347
9. Yadav T, Carrasco B, Serrano E *et al.* Roles of *Bacillus subtilis* DprA and SsbA in RecA-mediated genetic recombination. *J Biol Chem* 2014;**289**:27640–52. https://doi.org/10.1074/jbc.M114.577924
10. Kidane D, Carrasco B, Manfredi C *et al.* Evidence for different pathways during horizontal gene transfer in competent *Bacillus subtilis* cells. *PLoS Genet* 2009;**5**:e1000630. https://doi.org/10.1371/journal.pgen.1000630
11. Khemici V, Prudhomme M, Polard P. Tight interplay between replication stress and competence induction in *Streptococcus pneumoniae*. *Cells* 2021;**10**:1938.
12. Slager J, Kjos M, Attaiech L *et al.* Antibiotic-induced replication stress triggers bacterial competence by increasing gene dosage near the origin. *Cell* 2014;**157**:395–406. https://doi.org/10.1016/j.cell.2014.01.068
13. Johnston C, Martin B, Granadel C *et al.* Programmed protection of foreign DNA from restriction allows pathogenicity island exchange during pneumococcal transformation. *PLoS Pathog* 2013;**9**:e1003178. https://doi.org/10.1371/journal.ppat.1003178
14. Maier B. Competence and transformation in *Bacillus subtilis*. *Curr Issues Mol Biol* 2020;**37**:57–76. https://doi.org/10.21775/cimb.037.057
15. Oussenko IA, Sanchez R, Bechhofer DH. *Bacillus subtilis* YhaM, a member of a new family of 3′-to-5′ exonucleases in Gram-positive bacteria. *J Bacteriol* 2002;**184**:6250–9. https://doi.org/10.1128/JB.184.22.6250-6259.2002
16. Lipońska A, Lee H, Yap M-NF. Staphylococcal exoribonuclease YhaM destabilizes ribosomes by targeting the mRNA of a hibernation factor. *Nucleic Acids Res* 2024;**52**:8998–9013. https://doi.org/10.1093/nar/gkae596
17. Nye TM, Schroeder JW, Kearns DB *et al.* Complete genome sequence of undomesticated *Bacillus subtilis* strain NCIB 3610. *Genome Announc* 2017;**5**:e00364-17. https://doi.org/10.1128/genomeA.00364-17
18. Yasbin RE, Young FE. Transduction in *Bacillus subtilis* by bacteriophage SPP1. *J Virol* 1974;**14**:1343–8. https://doi.org/10.1128/jvi.14.6.1343-1348.1974
19. Koo B-M, Kritikos G, Farelli JD. *et al.* Construction and analysis of two genome-scale deletion libraries for *Bacillus subtilis*. *Cell Syst* 2017;**4**:291–305.e7. https://doi.org/10.1016/j.cels.2016.12.013
20. Guérout-Fleury AM, Frandsen N, Stragier P. Plasmids for ectopic integration in *Bacillus subtilis*. *Gene* 1996;**180**:57–61. https://doi.org/10.1016/S0378-1119(96)00404-0

21. Gibson DG, Young L, Chuang R-Y *et al.* Enzymatic assembly of DNA molecules up to several hundred kilobases. *Nat Methods* 2009;**6**:343–5. https://doi.org/10.1038/nmeth.1318
22. Burby PE, Simmons LA. CRISPR/Cas9 editing of the *Bacillus subtilis* genome. *Bio Protoc* 2017;**7**:e2272. https://doi.org/10.21769/BioProtoc.2272
23. Abramson J, Adler J, Dunger J. *et al.* Accurate structure prediction of biomolecular interactions with AlphaFold 3. *Nature* 2024;**630**:493–500. https://doi.org/10.1038/s41586-024-07487-w
24. Liebschner D, Afonine PV, Baker ML. *et al.* Macromolecular structure determination using X-rays, neutrons and electrons: recent developments in Phenix. *Acta Crystallogr D Struct Biol* 2019;**75**:861–77. https://doi.org/10.1107/S2059798319011471
25. Davis IW, Leaver-Fay A, Chen VB. *et al.* MolProbity: all-atom contacts and structure validation for proteins and nucleic acids. *Nucleic Acids Res* 2007;**35**:W375–83. https://doi.org/10.1093/nar/gkm216
26. Schindelin J, Arganda-Carreras I, Frise E. *et al.* Fiji: an open-source platform for biological-image analysis. *Nat Methods* 2012;**9**:676–82. https://doi.org/10.1038/nmeth.2019
27. Schroeder JW, Simmons LA. Complete genome sequence of *Bacillus subtilis* strain PY79. *Genome Announc* 2013;**1**:e01085-13. https://doi.org/10.1128/genomeA.01085-13
28. Dempwolff F, Sanchez S, Kearns DB. Tn*FLX*: a third-generation mariner-based transposon system for *Bacillus subtilis*. *Appl Environ Microb* 2020;**86**:e02893-19. https://doi.org/10.1128/AEM.02893-19
29. Loyo CL, Burton BM. Quantitative transformation efficiency assay for *Bacillus subtilis*. *Bio Protoc* 2018;**8**:e3109. https://doi.org/10.21769/BioProtoc.3109
30. Zinke M, Sachowsky KAA, Öster C *et al.* Architecture of the flexible tail tube of bacteriophage SPP1. *Nat Commun* 2020;**11**:5759. https://doi.org/10.1038/s41467-020-19611-1
31. Skutel M, Yanovskaya D, Demkina A *et al.* RecA-dependent or independent recombination of plasmid DNA generates a conflict with the host EcoKI immunity by launching restriction alleviation. *Nucleic Acids Res* 2024;**52**:5195–208. https://doi.org/10.1093/nar/gkae243
32. van Sinderen D, Luttinger A, Kong L *et al.* comK encodes the competence transcription factor, the key regulatory protein for competence development in *Bacillus subtilis*. *Mol Microbiol* 1995;**15**:455–62. https://doi.org/10.1111/j.1365-2958.1995.tb02259.x
33. Butala M, Zgur-Bertok D, Busby SJW. The bacterial LexA transcriptional repressor. *Cell Mol Life Sci* 2009;**66**:82–93. https://doi.org/10.1007/s00018-008-8378-6
34. Hör J, Garriss G, Di Giorgio S *et al.* Grad-seq in a Gram-positive bacterium reveals exonucleolytic sRNA activation in competence control. *EMBO J* 2020;**39**:e103852. https://doi.org/10.15252/embj.2019103852
35. Bechhofer DH, Deutscher MP. Bacterial ribonucleases and their roles in RNA metabolism. *Crit Rev Biochem Mol Biol* 2019;**54**:242–300. https://doi.org/10.1080/10409238.2019.1651816
36. Oussenko IA, Abe T, Ujiie H *et al.* Participation of 3′-to-5′ exoribonucleases in the turnover of *Bacillus subtilis* mRNA. *J Bacteriol* 2005;**187**:2758–67. https://doi.org/10.1128/JB.187.8.2758-2767.2005
37. Minazzato G, Gasparrini M, Amici A *et al.* Functional characterization of COG1713 (YqeK) as a novel diadenosine tetraphosphate hydrolase Family. *J Bacteriol* 2020;**202**:e00053-20. https://doi.org/10.1128/JB.00053-20
38. Jeon YJ, Park SC, Song WS *et al.* Structural and biochemical characterization of bacterial YpgQ protein reveals a metal-dependent nucleotide pyrophosphohydrolase. *J Struct Biol* 2016;**195**:113–22. https://doi.org/10.1016/j.jsb.2016.04.002
39. Tamman H, Ernits K, Roghanian M. *et al.* Structure of SpoT reveals evolutionary tuning of catalysis via conformational constraint. *Nat Chem Biol* 2023;**19**:334–45. https://doi.org/10.1038/s41589-022-01198-x
40. Langton M, Sun S, Ueda C *et al.* The HD-domain metalloprotein superfamily: an apparent common protein scaffold with diverse chemistries. *Catalysts* 2020;**10**:1191. https://doi.org/10.3390/catal10101191
41. Harlow LS, Kadziola A, Jensen KF *et al.* Crystal structure of the phosphorolytic exoribonuclease RNase PH from *Bacillus subtilis* and implications for its quaternary structure and tRNA binding. *Protein Sci* 2004;**13**:668–77. https://doi.org/10.1110/ps.03477004
42. Hartmann R, van Teeseling MCF, Thanbichler M *et al.* BacStalk: a comprehensive and interactive image analysis software tool for bacterial cell biology. *Mol Microbiol* 2020;**114**:140–50. https://doi.org/10.1111/mmi.14501
43. Redko Y, Condon C. Maturation of 23S rRNA in *Bacillus subtilis* in the absence of Mini-III. *J Bacteriol* 2010;**192**:356–9. https://doi.org/10.1128/JB.01096-09
44. Oliveira L, Tavares P, Alonso JC. Headful DNA packaging: bacteriophage SPP1 as a model system. *Virus Res* 2013;**173**:247–59. https://doi.org/10.1016/j.virusres.2013.01.021
45. Fang M, Zeisberg W-M, Condon C *et al.* Degradation of nanoRNA is performed by multiple redundant RNases in *Bacillus subtilis*. *Nucleic Acids Res* 2009;**37**:5114–25. https://doi.org/10.1093/nar/gkp527
46. Lécrivain A-L, Le Rhun A, Renault TT *et al.* *In vivo* 3′-to-5′ exoribonuclease targetomes of *Streptococcus pyogenes*. *Proc Natl Acad Sci USA* 2018;**115**:11814–9. https://doi.org/10.1073/pnas.1809663115

Received: March 13, 2025. **Revised:** April 14, 2025. **Editorial Decision:** April 16, 2025. **Accepted:** May 13, 2025